Chapter-2

Materials, Method, and Characterization Techniques

CHAPTER 2: Materials, Method, and Characterization Techniques

2.1 Overview

Details of the objective are explained in Chapter 1. It is essential to describe the method and characterization of the synthesis of materials applied with various tools, as well as to use experimental procedures for their properties and applications. The materials under consideration in the current study are (a) Copper lead Iodide ($CuPbI_3$) (b) Copper tin Iodide ($CuSnI_3$) (c) Cesium tin Iodide ($CsSnI_3$). All materials were prepared by the cold sintering method via solid-state reaction (SSR) method. The structural, thermodynamical, optical and electrical properties were studied for synthesizing materials. This chapter is divided into three sections:

(a) Synthesis of compounds: This section provides an explanation of material synthesis and the processing of compositions.

(b) Characterization techniques: This section delves into the characterization techniques for structural, thermodynamic, optical, and electrical properties providing detailed explanations of each method.

(c) Data analysis techniques: The section has included topics such as the use of Rietveld refinement for phase identification of materials, as well as discussions on electrical conductivity and impedance spectroscopy.

2.2 Description of the materials

Highly pure raw materials were employed in the synthesis of different perovskite compounds. Table 2.1 represents the specification of the materials with their chemical formula, purity and manufacturer details.

Table 2.1 Specifications of the raw materials

Sl. No	Raw Materials	Chemical Formula	Purity	Manufacturer
1.	Copper Iodide	CuI	99.999%	Sigma Aldrich
2.	Cesium Iodide	CsI	99.9%	Sigma Aldrich
3.	Lead Iodide	PbI_2	98%	Synthesize in Lab
4.	Tin(II) Iodide	SnI_2	99.2%	Alfa Aesar

Moreover, some reagents, chemicals, and solvents such as hydrochloric acid, dimethylformamide (DMF), nitric acid, lead nitrate, potassium iodide, ethanol, isopropanol, etc were also used to fabricate the compounds.

2.3 Synthesis of Materials

Perovskite materials (active materials) can be synthesized using a variety of techniques, including solvent engineering, one-step, two-step, and vapor-assisted solution procedures, etc[158][67][159]. The sample was synthesized in an ambient atmosphere conditions. As discussed in Chapter one, halide perovskites are not stable and are difficult to synthesize under ambient conditions. Thus, it's essential to understand the stability problem and the causes why it's challenging to synthesize these materials in the ambient atmosphere. According to the literature, the cold sintering approach. Which allows the material to be synthesized at ambient conditions, is the simplest and least expensive synthesis process when compared to other methods that have been reported. The solid-state reaction (cold sintering) synthesis method is discussed in detail in the next section.

2.3.1 Cold Sintering Method using the Solid State Reaction Method (SSR)

Cold sintering is a synthesis method that involves the low-temperature synthesis of materials, often at temperatures up to 200℃. In traditional sintering, synthesis progresses through phase formation, recrystallization, and grain growth. While in cold–sintering method, phase formation, recrystallization, and grain growth and development occurs up to 200℃ without any calcination[160]. Perovskite halides can be employed for synthesis since their nucleation temperature is lower than room temperature.

Principles of Cold Sintering:

Cold sintering involves the use of a transient liquid phase to facilitate the densification process. The key steps in cold sintering are[160][161][162]:

1.Material Preparation: The starting materials, typically in powder form, are generally mixed with a small amount of a liquid phase. This liquid can be water, an organic solvent, or an aqueous solution containing dissolved salts.

2.Compaction: The mixture is then compacted under uniaxial or isostatic pressure. This compaction helps to bring the particles into close contact, promoting the formation of necks between particles and the initial stages of densification.

3.Densification: The compacted mixture is subjected to a low-temperature heat treatment while maintaining the applied pressure. The liquid phase facilitates mass transport by dissolving and re-precipitating the material at particle interfaces, leading to densification. The liquid phase is then removed, typically by evaporation or decomposition, leaving behind a dense solid material.

Advantages of Cold Sintering:

1.Energy Efficiency

2.Enhanced Material Properties

3.Compatibility with a Wide Range of Materials

Applications of Cold Sintering:

Cold sintering has a broad range of potential applications in various fields:

Solar cells: Improved stability and efficiency of photovoltaic devices based on perovskites.

LEDs: Enhancing the efficacy and durability of light-emitting devices.

Sensors and Photodetectors: Developing sensitive and efficient sensors that detect light and other environmental elements.

Thus, cold sintering represents a transformative approach in materials science, offering a sustainable and efficient alternative to traditional high-temperature sintering. Its ability to densify materials at low temperatures opens up new possibilities for advanced materials and applications, paving the way for future technological advancements. This is particularly important for perovskite halides, as their nucleation temperature is lower than room temperature. Cold sintering emerges as the simplest and most cost-effective synthesis method compared to other reported techniques, providing good stability at normal ambient temperatures.Here in the current thesis copper lead halides and lead-free copper and cesium tin halides were synthesized using the cold sintering method under ambient conditions (Fig. 2.1).

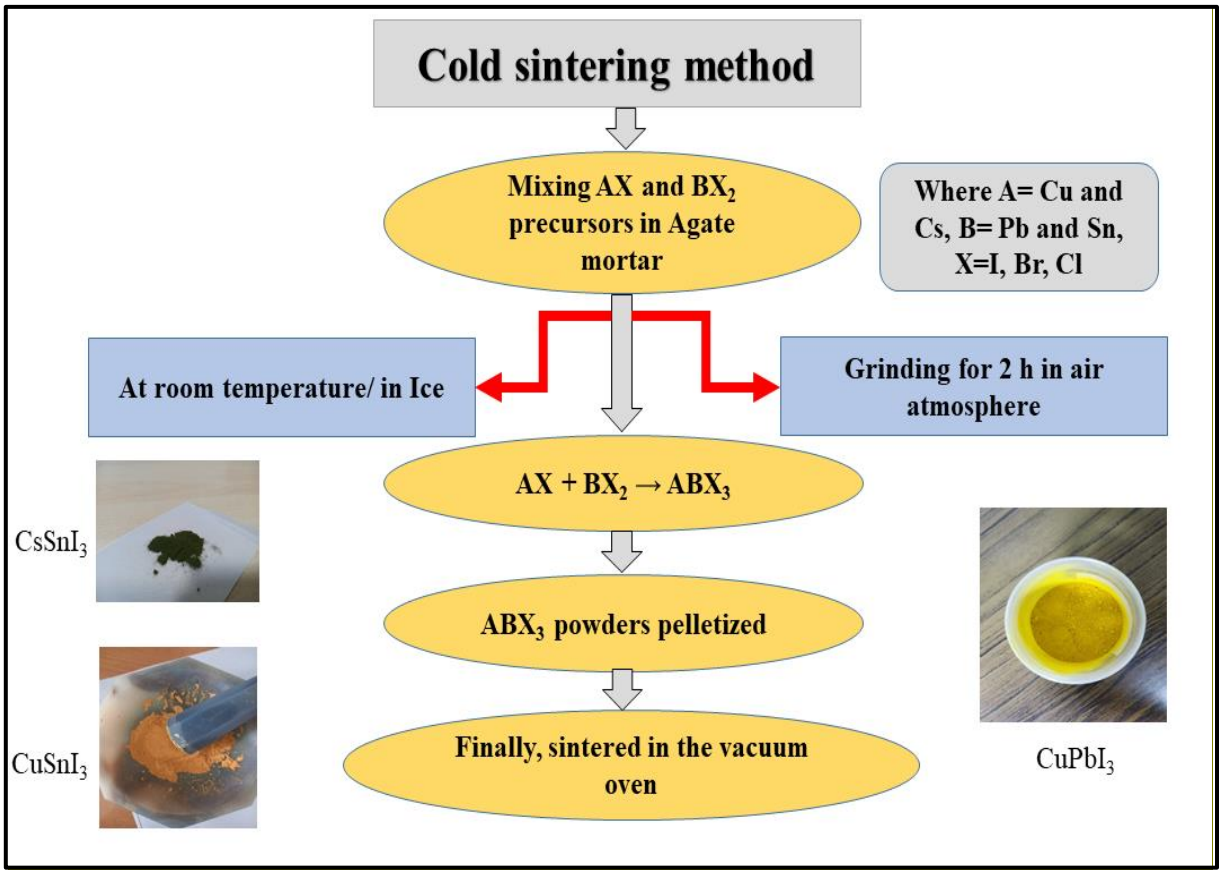

Figure 2.1 Flow chart of the cold sintering process for synthesizing perovskite samples.

For synthesizing the $CuPbI_3$, $CuSnI_3$ and $CsSnI_3$, the precursors of CuI, CsI, PbI_2 and SnI_2 has been weighted in stoichiometric ratio. To synthesize the particular compound, the required precursors in powder form were combined (Humidity, 35 %) in a pestle mortar and grounded for two hours at ice temperature and room temperature in ambient atmosphere. After grinding, The perovskite powder (active material) was pelletized using a hydraulic press at a pressure of 5 ton. Finally, pelletized samples were heated in a vacuum oven at different temperatures 100, 150 and 200℃ for 1 h. The precrusor PbI_2 synthesized in our lab for this the powder of lead nitrate $Pb(NO_3)_2$ and potassium iodide (KI) were weighed in stoichiometric ratio. The following is a chemical reaction.

$$Pb(NO_3)_2 + 2KI \rightarrow PbI_2 + 2KNO_3 \quad (2.1)$$

These two powders were mixed with distilled water in two separate beakers. Both the solutions were heated up to 100 ℃ at hot plate with the constant stirring rate 550 rpm. After that, both the solutions were mixed in new beaker and put for the natural cooling. After natural cooling yellow precipitate of PbI_2 (Figure 2.2) was formed, this precipitate was filtered and heated in vacuum oven for the 2 h at 100℃ to remove the water.

Figure 2.2 Yellow precipitate of lead iodide (PbI_2).

2.4 Characterization Techniques

2.4.1 Thermogravimetric Analysis (TGA)

The Idea of TGA was first time proposed by Japnease physicist Honda[163]. TGA(Thermo Gravimetric Analysis) is an important characterization technique which measures change in mass of a material with change in temperature. It works in two modes: 1) mass change is

observed as temperature (the scanning mode with constant heating rate); and 2) mass change is measured as time (the isothermal mode with constant temperature or constant mass loss). Both physical and chemical processes, including as absorption, sublimation, vaporization, oxidation, reduction, and decomposition, are responsible for this change in mass[164]. TGA is employed to find out the calcination temperature and thermal stability of a sample. A phase transition in the sample may also be confirmed by using this technique.

Working principle: During thermogravimetric analysis (TGA), a solid reactant undergoes decomposition upon heating, resulting in the formation of a product while simultaneously releasing gas. In this particular shift, there is a reduction in mass or weight. The mass loss can be attributed to the gas produced from the decomposition of reactants upon heating or the presence of H_2O with the reactants. It is possible to show the results of a thermogravimetric run in either the form of weight versus temperature or weight loss versus temperature according to this change. The resulting graph is commonly referred to as a thermogram. The plateau in the thermogram curve signifies a state of weight stability, whereas the curved portion suggests a decrease in weight.

The weight loss curve obtained from measurements provides valuable data on the thermal stability of the sample, variations in its composition, and kinetic factors. The derivative of the weight loss curve can be used to determine the point at which weight loss is most evident. A thermogravimetric analysis (TGA) consists of a sample pan that is connected to a precision balance.

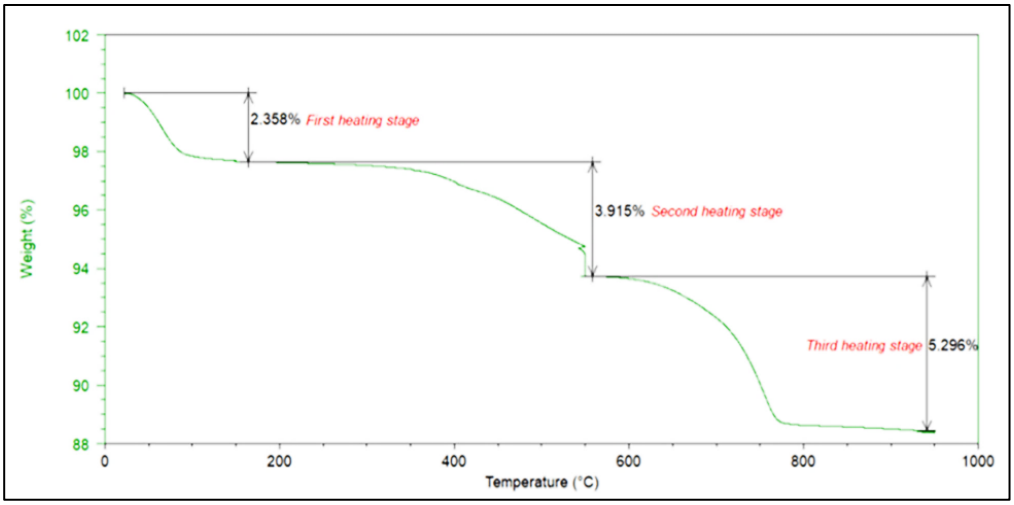

Figure 2.3 A thermogram curve showing the change of mass of a substance at different temperature [165].

That pan is either heated or cooled in a furnace while the experiment is being carried out. During the course of the experiment, the weight of the sample is measured. The sample environment is regulated by a sample purge gas.

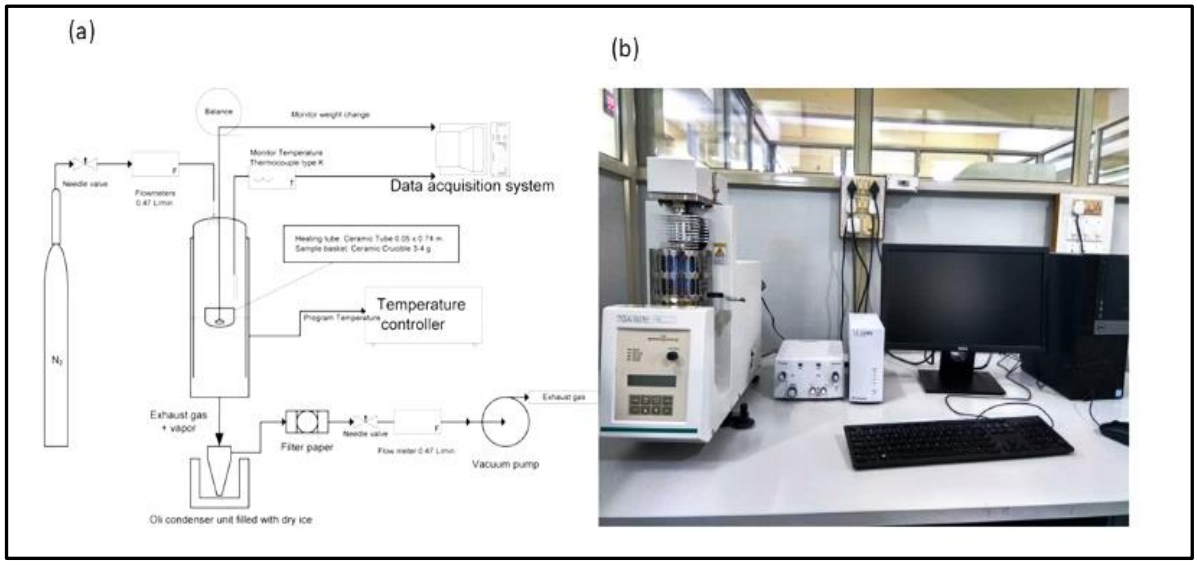

Figure 2.4 (a) Depicting the schematic diagram of TGA[166] (b) Experimental setup of TGA at Central instrument facility IIT(BHU).

The key components of a TGA apparatus include a highly accurate thermobalance, a furnace equipped with precise temperature control and programming capabilities, and the provision of either either an inert atmosphere or an oxidizing environment. For the current thesis work, TGA measurements were recorded using the Shimadzu TGA 50.

2.4.2 Differential Scanning Calorimetry (DSC)

Differential Scanning Calorimetry provides crucial information about the thermal transition of the material. Additionally, differential scanning calorimetry measures the amount of heat absorbed or emitted during the heating or cooling of the material to identify the exothermic and endothermic processes present in a sample [167]. It measures the difference in heat flow rate (mW) between material and reference as a function of temperature and time. During the experimental process, both the sample and the reference are kept at approximately the same temperature. The temperature program in this analysis is designed such that the temperature of the material holder increases linearly as a function of time and the reference sample should have well defined heat capacity over the entire range of temperatures that have to be scanned. It provides a curve of heat flux versus temperature or time. In the current thesis work, DSC measurement was recorded by SHIMADZU DSC-60 plus 230V. The various parameters such as entropy, enthalpy, type of reaction, specific heat, and Gibbs free energy of the samples were analyzed. DSC is used in a broad range of industries and research areas for the investigation of the melting point of crystals, glass transition, phase transition, crystallization temperatures, and chemical reactions, etc. The experimental setup and schematic diagram of the DSC technique depicts in (Figure 2.5).

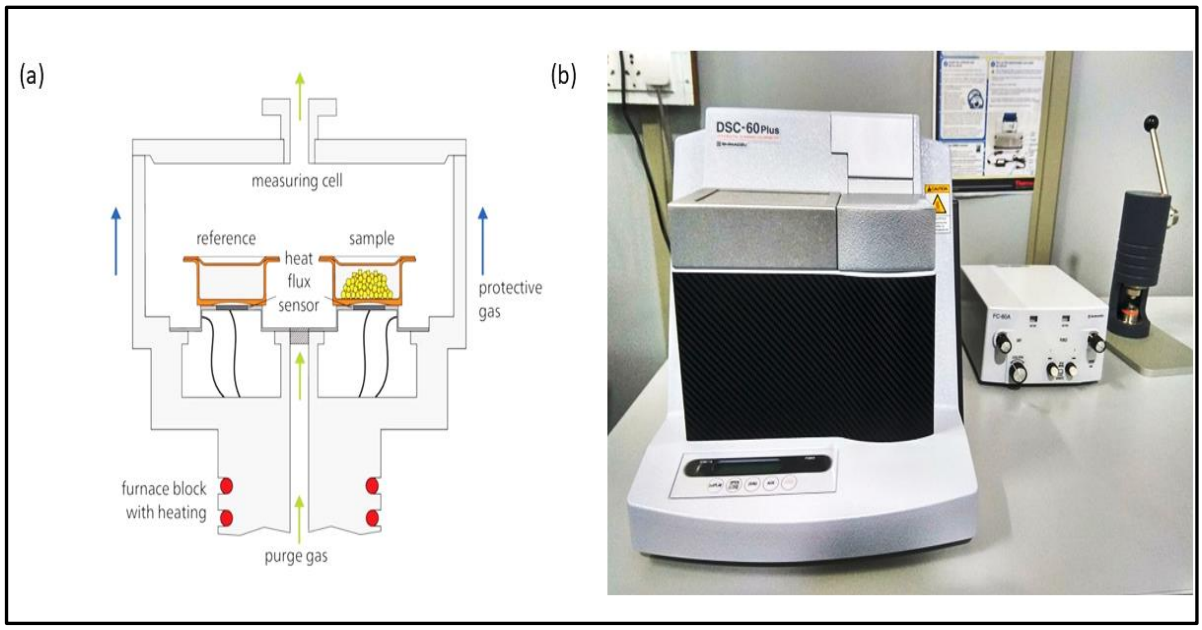

Figure 2.5 (a) Schematic diagram of DSC[168] (b) the experimental setup of DSC at CIF IIT (BHU).

There are two fundamental categories of differential scanning calorimetry (DSC), namely heat flux DSC and power compensation DSC. Heat flux differential scanning calorimeters (DSCs) operate by exchanging heat with the surrounding environment along a clearly defined path of heat conduction, which has a predetermined thermal resistance. In power compensation DSC, the heat being measured is mostly offset by electric energy through the adjustment of a Joule heater, either by increasing or decreasing its heat output. Both kinds of DSC share the characteristic that the measured signal is directly proportional to the rate of heat flow (ϕ), rather than the amount of heat, as is the case with most conventional calorimeters. The $\phi(t)$ curve can be used to identify the time variations of a transition. Directly measured heat flow rates are this feature that allows all DSCs to solve problems in a variety of applications[167].

Working principle: In a differential scanning calorimeter (DSC), the initial quantities that are measured are a temperature difference, which is expressed as a voltage, and the temperature of the furnace (or sample support) that has been defined. The difference in temperature is

transformed into a differential heat flow rate by the process that occurs internally. The DSC curve is produced by the unprocessed data that is collected and serves as the foundation for all subsequent investigations. The DSC curve can be utilised to rapidly ascertain accurate heat variations, transitions, and reactions. The estimation of various thermodynamic functions can be achieved from a differential scanning calorimetry (DSC) curve by utilising the following equations:

$$C_V = \frac{dQ}{dT} \tag{2.2}$$

$$\Delta G = \Delta H - T\Delta S \tag{2.3}$$

$$\Delta S = \frac{C_V}{T} \tag{2.4}$$

$$K = e^{-\Delta G/RT} \tag{2.5}$$

The variables in the given equations are as follows: $C_V$represents specific heat, *Q* represents heat flow, *T* represents temperature in Kelvin, *S* represents entropy, *G* represents Gibb's free energy, *H* represents enthalpy, *K* represents the equilibrium constant for reaction kinetics, and *R* represents the universal gas constant. The results obtained via DSC can be applied to address a wide range of issues. It can be utilised for measuring heat capacity, determining heat of reaction, investigating kinetics, studying the glass transition process, analysing phase behaviour, and determining phase diagrams.

2.4.3 X-Ray Diffraction (XRD)

Phase confirmation for the synthesized samples was carried out by X-ray diffraction (XRD), which allows for the investigation of phase formation as well as other structural parameters

such as average grain size and crystallinity. It is a non-destructive and versatile analytical technique in which the materials can also be exposed to different temperature and pressure conditions during the collection of the diffraction pattern [169].When a monochromatic beam of X-ray is incident on the sample, the incident X-ray photons are interact to the electrons of an atom in the sample as a result some of the photons are diffracted away from their original incident direction. Diffraction is the phenomenon in which the electromagnetic wave bend form an obstacle if the size of obstacle is comparable to wavelength of wave. An inter-atomic distance in crystalline materials lies in the range of 1 to 10 Å which is the same order of X-ray wavelength. There are only certain directions in which diffracted wave interfere constructively and interference peaks are observed for a particular crystalline solid at particular angles. Atoms are arranged periodically in the crystals, if the interference occurred by diffracted waves from the atomic planes satisfy Bragg‘s condition then it gives the X-ray diffraction pattern of a given material by measuring the intensity of diffracted waves with variation of the X-ray incident angle. XRD technique is not only identify the phase of synthesized sample, but also provides the information of crystal structure and the dimension of unit cell.

Bragg’s Law:

A relation between inter-atomic distance ‘d_{hkl}’, wavelength of the incident beam ‘λ’ and angle of incident beam ‘θ’ has been given by W. Lawrence Bragg and William H. Bragg, known as Bragg‘s law[170].

Consider a set of crystallographic lattice planes with an interplanar spacing d_{hkl} is irradiated by a plane wave X-ray. Let be the angle of incidence between X-ray beam and lattice plane, the interplanar spacing creates a path difference for the ray scattered from the top & bottom

surface of the plane. Using the geometry, the path difference between incident and iffracted ray is found to be $2d_{hkl}sin\theta$. If the path difference is an integral multiple of wavelength (λ), then the interference between the scattered rays can be said to be constructive.

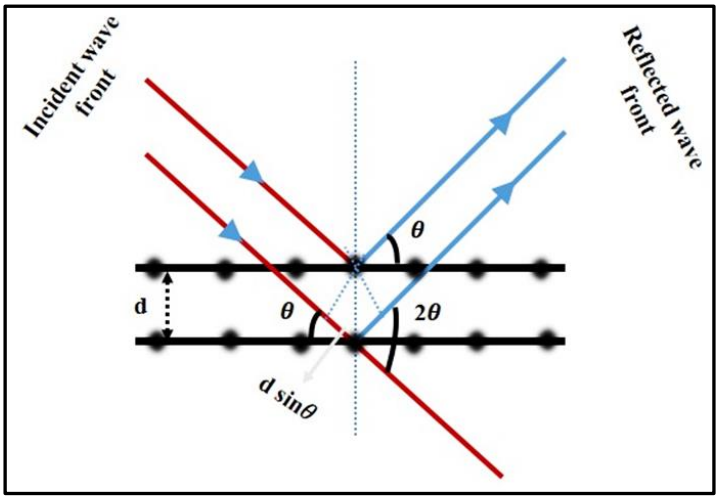

Figure 2.6 Illustration of Bragg's law X-ray diffractometer.

Mathematically Bragg's law is given as:

$$2d_{hkl}sin\theta=n\lambda \quad (2.6)$$

Where *n* is integer, representing the order of diffraction, *hkl* are miller indices of a particular planeand *d* is inter-planer spacing,

Bragg-Brentano geometry:

Figure 2.7 illustrates the fundamental geometry employed in the majority of X-ray diffractometers. The angle between the incident ray and the scattered ray in relation to the surface of the specimen is denoted as θ. The XRD pattern is created by adjusting the incidence angle of the X-ray beam by θ and the scattering angle by 2θ . Ultimately, the intensity (I) has been measured and recorded as a function of 2θ . In certain situations, the X-ray source is

stationary while the sample rotates by angle θ and the detector moves by 2θ . Furthermore, in the majority of instances, the sample remains stationary while both the X-ray source and the detector are rotated simultaneously at an angle θ .The goniometer, which is the central component of the diffractometer, is responsible for performing this precise rotation. Typically, the sample is positioned on the rotational axis, while the X-ray source and detector rotate around the perimeter.

Phase Matching:

The peaks in the powder XRD pattern are produced by the randomly orientated planes that are designated by the respective Miller indices. The XRD peaks are matched and indexed using a standard phase identification method that takes into account crystallographic information such as relative intensity, interplanar spacing, diffraction angles, and Miller indices[171]. The primary database is managed by the **"International Centre for Diffraction Data (ICDD)"** previously referred to as the **"Joint Committee for Powder Diffraction Standards (JCPDS)."**

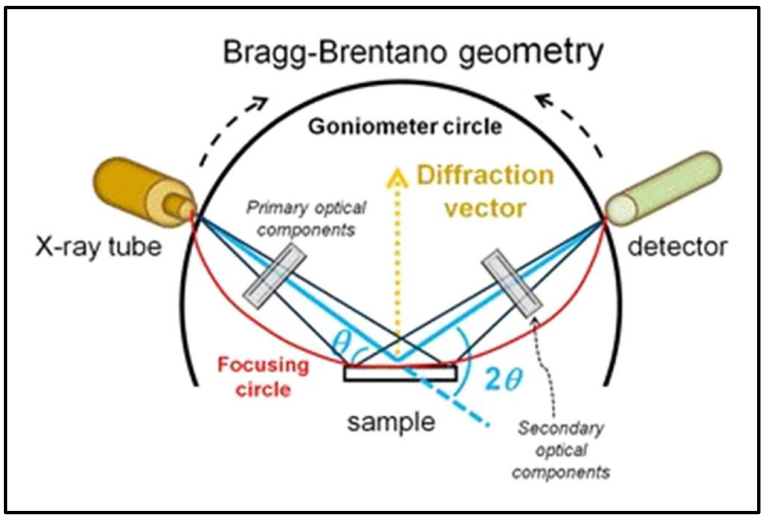

Figure 2.7 Schematic representation of θ⁄2θ diffraction in Bragg-Brentano geometry [172].

In the present thesis, the experimental XRD pattern is compared to the ICDD database. This approach can only be used if the crystal phase(s) or a comparable structure file is included in the ICDD database. The initial XRD pattern is refined through an iterative process, where various instrumental, structural, and microstructural parameters are adjusted to match the experimental XRD pattern[173].

The intensity vs 2θ data was recorded using the Rigaku-Miniflex II DESKTOP powder X-ray diffractometer (figure 2.8). This diffractometer has a monochromatic X-ray source with CuKα radiation (λ=1.5418 Å).The XRD data were recorded with a slow-scanning rate (2 degree/minute) in a step size of 0.01 degree with an applied voltage of at 30 kV and 15 mA.

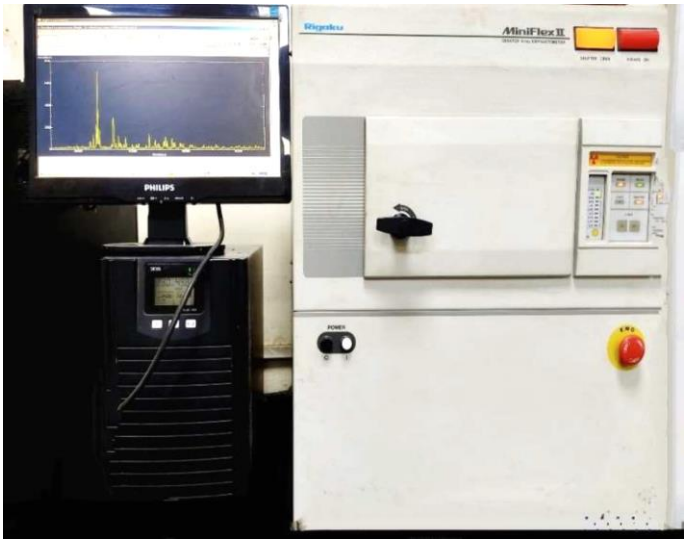

Figure 2.8 X-ray diffractometer (Rigaku-Miniflex II DESKTOP), Deapartment of Physics IIT (BHU).

2.4.4 Scanning Electron Microscope (SEM)

Scanning electron microscopy (SEM) is a valuable technique used to analyse the morphology of a material, surface characterization and examine metal particles' size at the nano to

microlevel scale. SEM utilizes a highly focused electron beam to produce the image of the sample , When a high-energy electron beam collides with a sample's surface, it causes a variety of interactions that reveal details about the sample's chemical composition and morphology[174]. Figure 2.9 illustrates the different electron-sample interactions. For the electron beam to pass through the sample, the sample should be conductive. So in the case of nonconducting samples, a layer of gold is deposited on the surface of the sample SEM is the most commonly used microscopic method because of its uncomplicated sample preparation and easy handling. First scanning electron microscope constructed by Mafred von Ardenne in 1937[175].

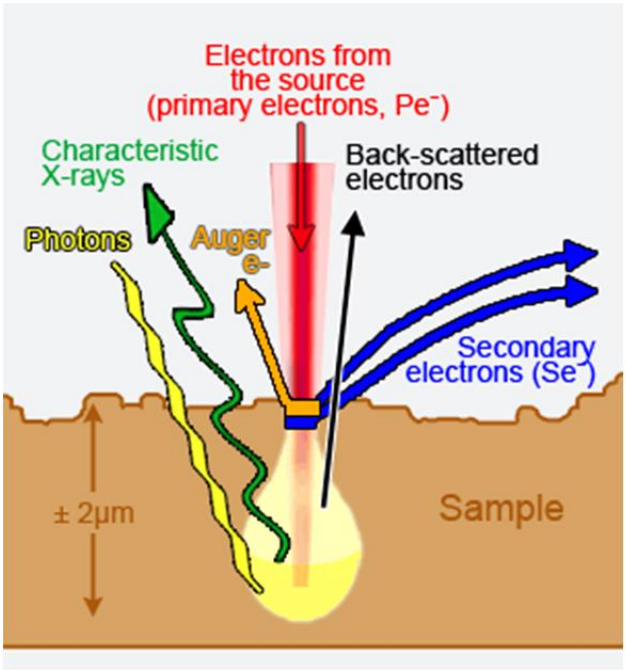

Figure 2.9 The interaction of the electron beam with the sample [176].

The spatial resolution of a scanning electron microscope (SEM) can range from 50 nm to 100 nm, depending on the magnification level, which can vary from 20X to about 30,000X. Nevertheless, some scanning electron microscopes (SEMs) are capable of achieving

resolutions higher than one nanometre.In addition, the Energy-dispersive X-ray analysis (EDAX or EDX) is used to analyze the elemental compositional analysis. It uses X-ray analysis to examine the elemental composition of any material up to 0.5 - 1 atomic percent sensitivity.

The main components of the Scanning Electron Microscope are: Electron Source(gun), Lenses, Scanning Coil, Detector, display device,Power source and Vacuum system.

Working Principle:

The scanning electron microscope (SEM) uses a focused beam of high-energy electrons to produce a variety of signals on the surface of solid specimens. The source generates a consistent flow of electrons. An electron gun fires an electron beam at the object under examination. Essentially, there are two types of electron gun used in scanning electron microscopy (SEM). The most prevalent variety is the thermionic gun, which generates electrons by applying thermal energy to the tungsten filament. Another type is field emission guns, which generate a strong electrical field that pushes electrons away from the atoms to which they are attached. Afterward, the electrons undergo acceleration to a voltage range of 1-40 kV. The lenses then focus and control the electron beam, ensuring that the electrons impact precisely where they are intended. The samples are mounted and placed in an evacuated chamber. In a scanning electron microscope (SEM), high-energy electrons possess significant kinetic energy, which is converted into various signals due to interactions between the electrons and the sample. These interactions occur as the incident electrons slow down within the solid sample. The signals consist of secondary electrons (SE), backscattered electrons (BSE), diffracted backscattered electrons (EBSD), visible light, photons, and heat. Among these signals, two signals are primarily detected in SEM. These are secondary and backscattered

electrons. Secondary electrons are better for showing sample morphology and topography, while backscattered electrons are best for showing compositional variations in multiphase samples [177]. Several phenomena take place when an electron beam interacts with a sample in a scanning electron microscope (SEM). Various detectors are necessary to distinguish between secondary electrons, backscattered electrons, and unique x-rays. Detectors capable of detecting secondary electrons have the ability to produce highly detailed images of an object's surface. Other detectors, such backscattered electron detectors and X-ray detectors, can provide information about a substance's composition. When the inner vacant electron position is filled by an outer electron, the energy difference can be released in the form of X-rays. Based on the energy of this emitted X-ray, information about the elements of the sample can be obtained. EDAX provides semi-quantitative and qualitative information of the elements present in any composition. Scanning Electron Microscopes (SEMs) are utilised in various industrial, commercial, and scientific research applications..

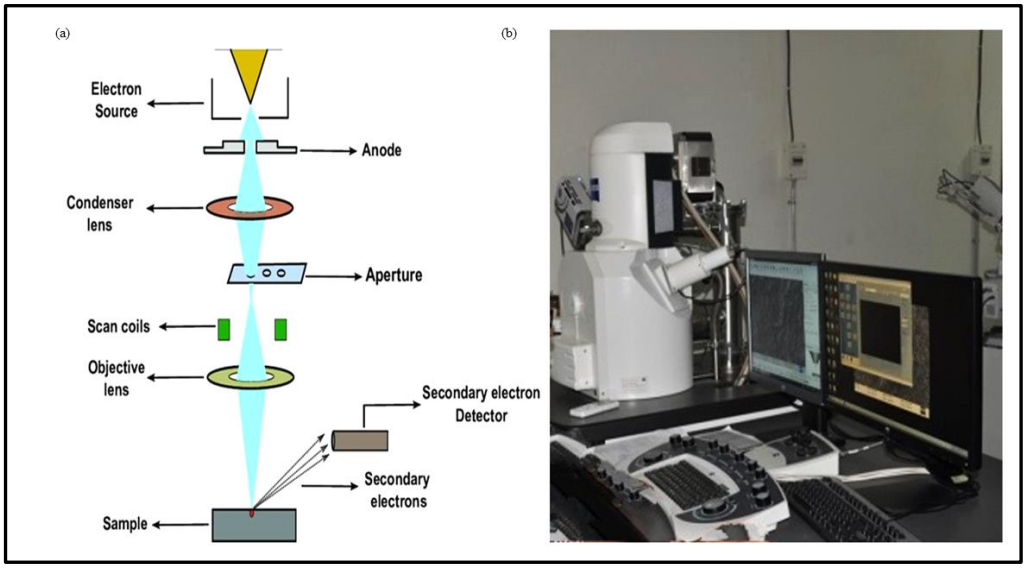

Figure 2.10 (a) Working Principal of SEM [178] (b) Experimental setup of SEM measurement (CIF-IIT (BHU)).

The SEM is employed to generate high-resolution images of objects and to demonstrate spatial changes in chemical compositions, such as performing spot chemical analyses using EDS or the creation of elemental maps. Scanning electron microscopes (SEMs) are widely employed in contemporary materials science research to analyse and study various materials such as nanotubes, nanofibers, high temperature superconductors, mesoporous structures, and alloy strength. Actually, scanning electron microscopes have made possible nearly every industry related to materials science, including aerospace, chemistry, electronics, and energy utilisation

In the present thesis work, SEM and EDS were recorded using EVO - Scanning Electron Microscope MA15/18, and EDS is investigated by 51N1000 – EDS System represented in Fig. 2.10(b).

2.4.5 Raman Spectroscopy

Raman spectroscopy is an analytical method used to identify various materials, including liquids, gases, and solids. This technique involves measuring the vibrational energy mode of a sample by analysing the scattered light. The technique provide both structural and chemical data, along with the ability to identify materials based on their distinctive Raman 'fingerprints'[179]. The “Raman spectroscopy” is based on the scattering of light through a matter. Historically, after the discovery of Compton scattering in 1923, where X-ray is scattered by electrons and the wavelength of the X-ray is changed, C. V. Raman though the optical analogue of Compton effect and ultimately in 1928, Raman with his research partner Krishan was able to discover the Raman spectroscopy. When Raman did his first, he used sunlight as a source and his naked eye as a detector, due to unavailability of advanced instrumentation. Afterwards, the light was allowed to fall on a photographic plate. Later on, a

lot of improvements have been made like invention of a good excitation source with advanced detector and a commercial Raman spectrometer was accessible. And this spectroscopy become an innovating technique to probe the qualitative and quantitative dynamic of atoms/ions/molecules in crystal using the scattering of light. While light scattering from the molecule/crystal, the most of photons get elastically scattered. The elastically scattered photons will possess the same energy as the incident photons. There is a very small fraction of light (~1 photon out of 10^7 photons) which gets inelastically scattered with a change in their wavelengths by changing by changing rotational/vibrational/electronic energy of the molecule. This inelastic scattering is known as the famous Raman Effect (i.e., usually described as Raman shift) and the elastic scattering is recognized as Rayleigh scattering.

Working Principal:

The phenomena of Raman effect can be explained based on the deformation of molecules in an electric field of strength E owing to the induced electric dipole moment, $P = \alpha E$ (α is the polarizability). The Raman shift can be observed only the derivative of α is non-zero with respect to Q (normal co-ordinates). When electromagnetic radiation interacts with the atom/molecule the electron clouds and bonds of the molecules get distorted. Due to this interaction, the atom/molecule get excited to a virtual energy state from their ground state thus becomes unstable. These excited molecules returns to a different stable state (rotational or vibrational) by decreasing their energy through releasing a photon. The difference in energy of initial stable state and final stable of the molecule cause shifting of the frequency of the emitted photon from the excitation energy. If the final state has large energy, then the we get a emitted photon of a lower frequency than the excitation frequency and this shifting of energy.

Block diagram of Raman spectrometer is shown in figure 2.11(a) which has four major components: (i) Excitation source (LASER) (ii) Sample illumination system (iii) Light collecting optics, wavelength selector (Filter, spectrophotometer) (iv) Detector (Photodiode array, CCD or Photo-multiplier-tube(PMT)). Typically, the sample is illuminated by a laser beam of ultra-violet (UV) or visible (Vis), or near-infrared range (NIR) available with a spectrometer.

The Raman effect can be explained by the molecular deformation that occurs in the presence of an electric field with strength E, resulting in the generation of an electric dipole moment, $P = \alpha E$ (where α represents the polarizability). The Raman shift can only be noticed when the derivative of α is non-zero with respect to Q (normal coordinates). When electromagnetic radiation interacts with an atom/molecule, the electron clouds and bonds of the molecules become deformed.

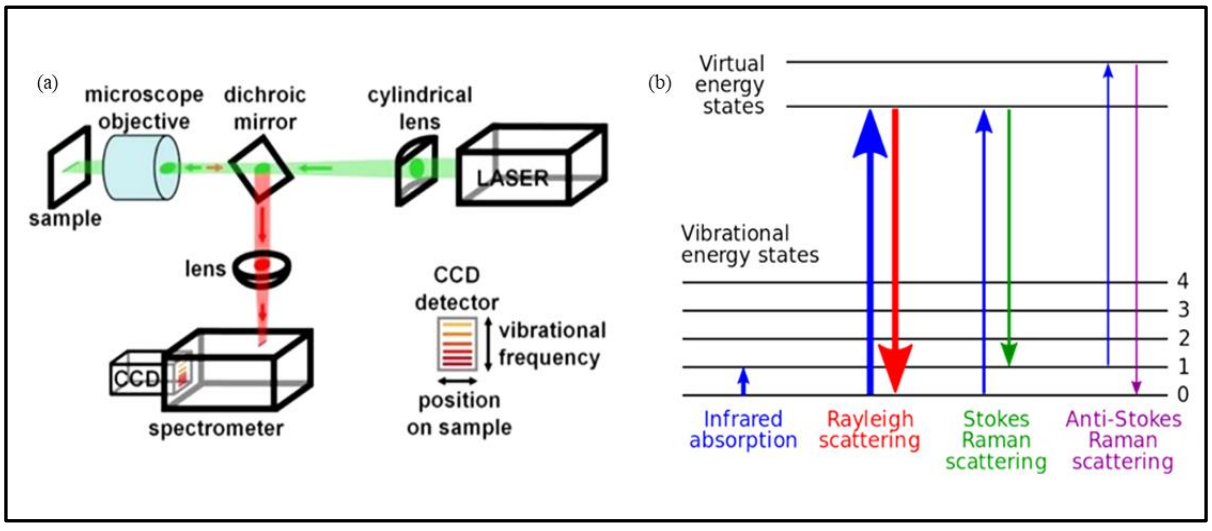

Figure 2.11 (a) Components of raman spectrograph[180] (b) representation of the principle of Raman spectroscopy[181].

As a result of this interaction, the atom/molecule becomes excited to a virtual energy state from its ground state, leading to instability. These excited molecules return to a distinct stable state (rotational or vibrational) by emitting a photon, which reduces their energy. The difference in energy between the initial stable state and the final stable state of the molecule results in a change in the frequency of the emitted photon from the excitation energy. If the final state possesses a significant amount of energy, the result is the emission of a photon with a frequency lower than that of the excitation frequency.

This phenomenon, in which the energy of the scattered photon is altered, is referred to as the Stokes shift (Figure 2.11(b)). On the other hand, when the final state has lower energy, we observe a higher energy emitted photon, which is known as the Anti-Stokes shift.

Figure 2.12 Experimental setup of LabRAM HR Evol Raman spectroscope.

The Raman spectra are often expressed in terms of wave numbers in units of inverse of length (cm-1). The Raman spectra of the powders were detected using a LabRAM HR Evol Raman spectrometer in the thesis work which is shown in figure 2.12. Here, a monochromatic laser

light with a wavelength of 633 nm and 785nm were utilized. To avoid heating of the specimen, only 5% power was allowed to incident on the sample.

2.4.6 Ultra-Violet Visible (UV-Vis) Spectroscopy

UV-Vis spectrometers are now the most widely used analytical instruments for examining the optical characteristics of materials because of their affordability, ease of use, accuracy, speed, and variety. One can observe this phenomenon by utilising UV-Vis spectroscopy to analyse the absorption and reflection of samples within the ultraviolet and visible spectral region. Furthermore, the bandgaps of the samples (thin films, bulk powders, liquids) have been estimated based on the UV-Vis data[182].

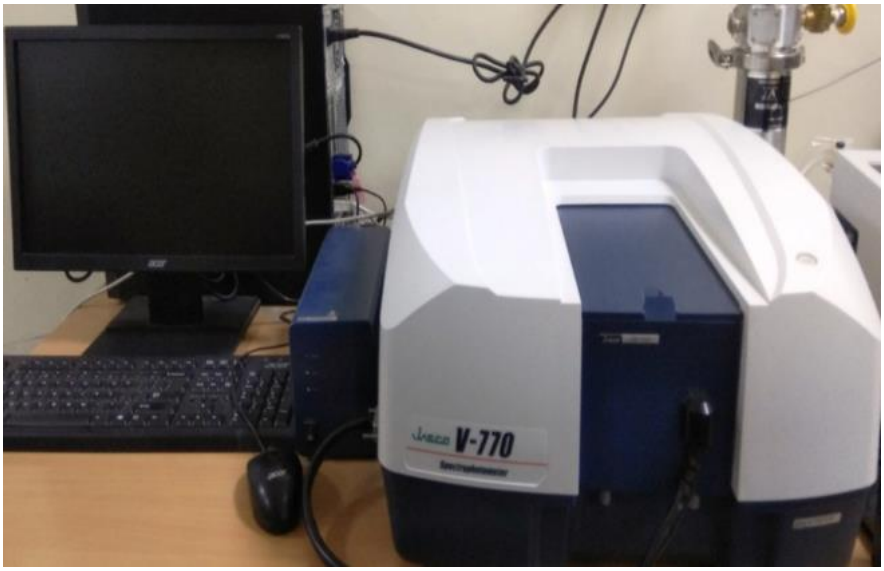

Figure 2.13 Experimental setup of JASCO V-770 UV-Vis spectrometer

The fundamental concept governing the workings of UV/Vis/NIR spectroscopy is Beer-Lambert's law. It is defined as the linear relationship between the concentration and absorbance of an absorbing material. It is given by

$$A = \log_{10}\left(\frac{I}{I_0}\right) = \varepsilon \times \ell \times c \qquad (2.7)$$

The variables A, ε, l, and c represent the absorbance, wavelength-dependent absorptive coefficient, path length, and material concentration, respectively. Furthermore, I_0 and I represent the intensity of incident light and transmitted light, respectively. The spectrophotometer contains four major components: (a) sample holder (b) light source (c) diffraction grating of monochromator (d) detector. The Jasco V-700 spectrophotometer consists of two radidation sources , a deuterium lamp as a UV source (190nm to 400nm) and a Halogen as visible and NIR source(300nm to 2500nm). The radiation source worked in continuous mode for visible wavelengths. The charge-coupled device (CCD), also known as a photodiode, and photomultiplier tube acts as detectors. Photomultiplier tubes and single photodiode detectors are used to scan the monochromator. The device selectively blocks all wavelengths except for one, particular wavelength to reach the detector. In order to quantify the intensity of a light as a function of wavelength, the diffraction grating enables the "step-across" transfer of each wavelength through scanning the monochromator. The absorption edge in the visible region has been observed in all samples in the current study. The JASCO V-770 ultraviolet-visible (UV) spectrometer has been used to capture the optical absorption spectra (Figure 2.13). The Tauc equation has been used to estimate the bandgap of the samples[183]

$$(\alpha h\nu)^{1/n} = A\left(h\nu - E_g\right) \qquad (2.8)$$

The variables E_g, α, A, and hν represent the optical band gap, energy absorption coefficient, an energy-independent constant, and incident photon energy respectively. The exponent n represents the characteristics of a transition, indicating whether it is allowed or forbidden, as well as whether it is direct or indirect. n = 1/2 corresponds to direct allowed transition, n = 3/2

corresponds to direct forbidden transition, n = 2 for indirect allowed transition and n = 3 for indirect forbidden transition.

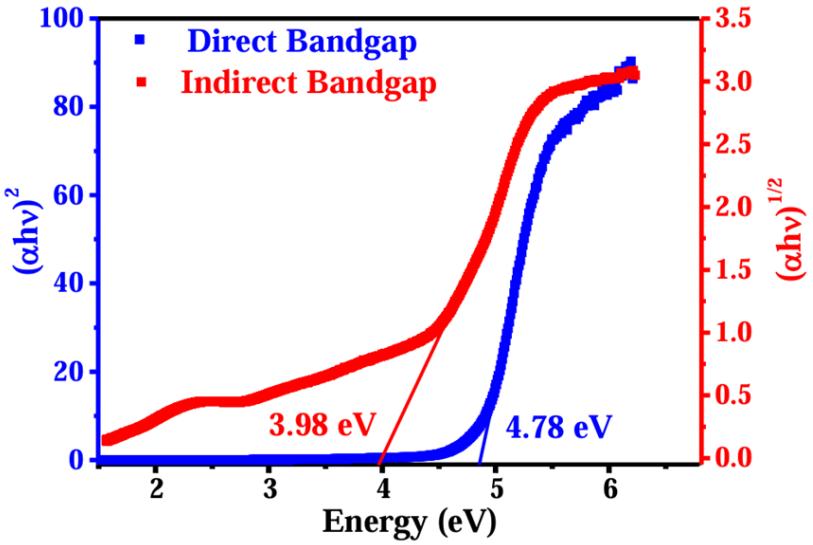

Figure 2.14 Tauc plot generated by Tauc equation.

The band gap corresponding to direct transition was obtained by extrapolating the linear portion of $(\alpha h\nu)^2$ verses $h\nu$ curves such that $(\alpha h\nu)^2 = 0$.The typical plot of $(\alpha h\nu)^2$ vs $h\nu$ is shown in figure 2.14.

Urbach Energy:

In semiconductors, there are various mechanisms for light absorption, including interband absorption, absorption by free charge carriers, absorption by the crystalline lattice, dopant absorption, excitonic absorption, and weak tail absorption. The fundamental absorption (interband absorption) generates electron-hole pairs by optically excitating electrons from the valence band to the conduction band, which is the semiconductor's band gap.

The Urbach Energy, also known as the Urbach Edge, is a parameter that is used to measure the energetic disorder in the band edges of a semiconductor. It is usually given in terms of energy. An exponential function is used to fit the absorption coefficient as a function of energy in order to determine its value. Franz Urbach systematically examined this characteristic in crystals. He conducted his research on silver bromide while working at the Kodak Company in 1953.

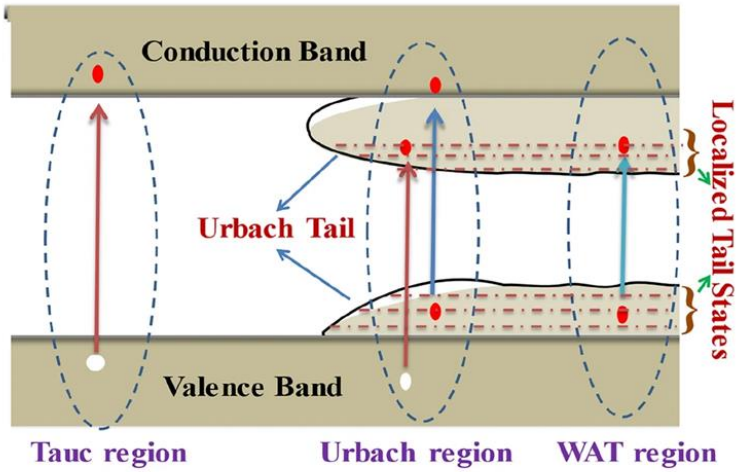

Figure 2.15 Graphical representation of the valence and conduction bands and band tail (urbach energy) [184].

The Urbach tail is an exponential portion that appears near the optical band edge and along the absorption coefficient curve. This exponential tail is observed in materials that are low crystalline, poor crystalline, disordered, and amorphous. This is due to the fact that these materials have localised states that extend in the band gap. The following equation gives the Urbach empirical rule, which describes the spectrum dependency of the absorption coefficient (α) and photon energy (hv) in the low photon energy range:

$$\alpha = \alpha_0(h\nu - E_g/E_U) \tag{2.9}$$

Where α_0 is a constant, α is the absorption coefficient, E_g band gap and E_U denotes the energy of the band tail, known as Urbach energy, which is weakly dependent on temperature and is often interpreted as the width of the band tail due to localised states in the normally band gap that is associated with disordered or low crystalline materials.

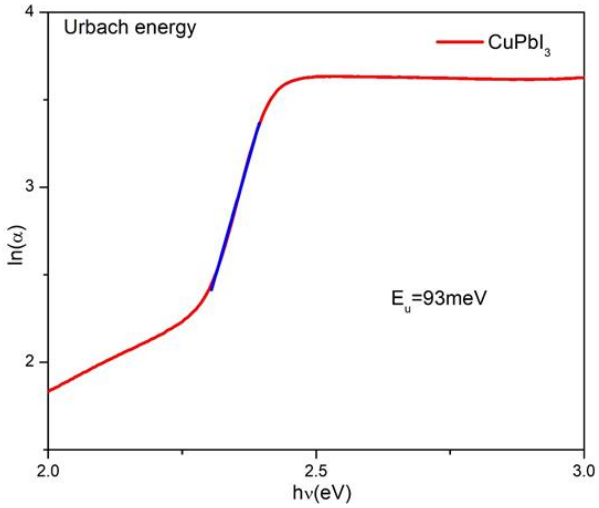

Figure 2.16 Estimation of Urbach energy.

By taking the logarithm of the above equation's two sides, we can get an equation for a straight line. It is given as follows:

$$ln\alpha = ln\alpha_0 + (h\nu/E_U) \tag{2.10}$$

Therefore, the band tail energy or Urbach energy (E_U) can be obtained from the slope of the straight line of plotting $ln\ (\alpha)$ against the incident photon energy ($h\nu$).

2.4.7 Atomic Force Microscopy/ Piezoforce Microscopy (AFM /PFM)

2.4.7.1 Introduction:

The Atomic Force Microscope is a type of scanning probe microscope that uses the interactions between a tip and a sample surface to create a topographical image of the sample surface. In 1986, Gerd Binning et al. at IBM Zurich developed the atomic force microscope, building upon the scanning tunnelling microscope (STM) that had been introduced in 1981. Despite the fact that the latter is dependent on the conductive samples, the AFM supports the utilisation of non-conductive samples as well. In recognition of their accomplishments, the inventors were granted the Nobel Prize in Physics in 1987.

Modern atomic force microscopy (AFM) offers a versatile approach to non-destructive surface profilometry with a resolution greater than 1 nm, and perhaps even better.At the atomic scale, the device is capable of detecting extremely small forces, ranging from 10^{-2} to 10^{-8} Newtons, between the tip and the surface of the specimen, depending on the distance. The schematic of atomic force microscope is seen in the figure 2.18(b).

An atomic force microscope (AFM) consists of several essential elements such as Probe tip,Cantilever, Optical microscope, Laser source, Sample stage, Piezoelectric scanner, Position sensitive photodiode, Feedback control loop, and Computer .

Working Principal:

The AFM measures the forces that exist between a tiny tip and a sample.A pointed V-shaped probe is attached to the tip of a flexible microcantilever arm [185]. The interatomic potentials between the atoms of the tip and the atoms of the surface are created when the tip is brought

inside the interatomic gap between the tip and the sample. These potentials can result in either attracting or repulsive forces depending on the nature of the interatomic potential. The force between the tip and the sample fluctuates as it scans the sample's surface, and the tip senses this variation. The force between the probe and the sample is proportional to the cantilever's spring constant and the distance between the probe and the surface. This force can be described using Hooke's Law.

$$F = -\mathrm{kx} \tag{2.11}$$

Where F, k and x represents force, spring constant and cantilever deflection.

If the spring constant of the cantilever, which is normally around 0.1-1 N/m, is lower than that of the surface, the cantilever will bend and the deflection will be measured. The probes and cantilevers are primarily constructed from silicon nitride or silicon due to their exceptional mechanical stability. The top surface of the cantilever is coated with a thin layer of reflective material, commonly composed of either gold or aluminium. A laser beam is directed towards the cantilever and then bounces back onto a photodetector that can detect the position of the beam. Any deviation of the cantilever results in a shift in the laser spot's location on the photodetector, which may be detected[186]. The probe can be systematically moved across the surface of the specimen using a raster scanning technique. This allows for the creation of a three-dimensional picture, which provides detailed information on the relative heights of different parts of the sample.

Different scanning modes are used to probe the force scanning the sample surface:

Contact mode: During contact mode, the tip makes direct and gentle contact with the surface.The movement is significantly impacted by adhesive and frictional forces, which have

the potential to cause damage to the sample. The force exerted on the tip is repulsive. An picture of the surface can be obtained by keeping the optical lens cantilever deflection constant (via feedback loops), which in turn keeps the force between the probe and the sample constant.

Non-contact mode: The scan is performed by lifting the probe by at least one nanometer from the sample surface

Intermittent contact mode (tapping mode): This imaging method is similar to contact mode. But, in this mode, the cantilever oscillates at its resonant frequency and gently "taps" on the sample surface during scanning, thus contacting the sample surface at the bottom of its swing. A constant tip-sample interaction is maintained by maintaining a constant oscillation amplitude, and a digitized image of the sample surface is thus gained.

Piezoresponse force microscopy, often known as PFM, is a subtype of atomic force microscopy (AFM) that enables the imaging and manipulation of piezoelectric and ferroelectric material domains. his is accomplished by bringing a sharp conductive probe into contact with a ferroelectric surface (or piezoelectric material) and delivering an alternating current (AC) bias to the probe tip in order to trigger deformation of the sample via the converse piezoelectric effect (CPE).

The deflection of the probe cantilever is detected using normal split photodiode detector methods and then demodulated with a lock-in amplifier. PFM is commonly used for several purposes, such as analysing the electromechanical properties of ferroelectric materials . This includes carrying out comprehensive domain mapping and studying the dynamics of domain switching, which may be visualised through the material's ferroelectric hysteresis.

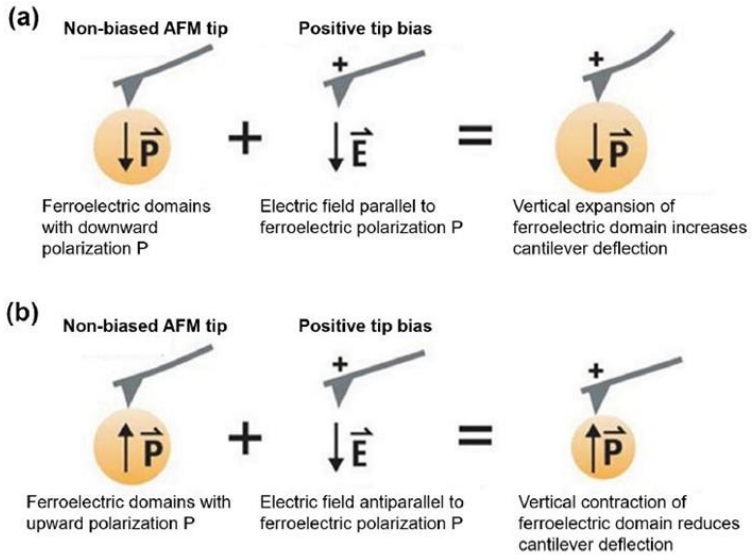

Figure 2.17 Basic concept of PFM, (a) downward polarization and (b) upward polarization of ferroelectric domains[187].

In the present thesis, PFM data is obtained using the NTEGRA Prima scanning probe microscope.

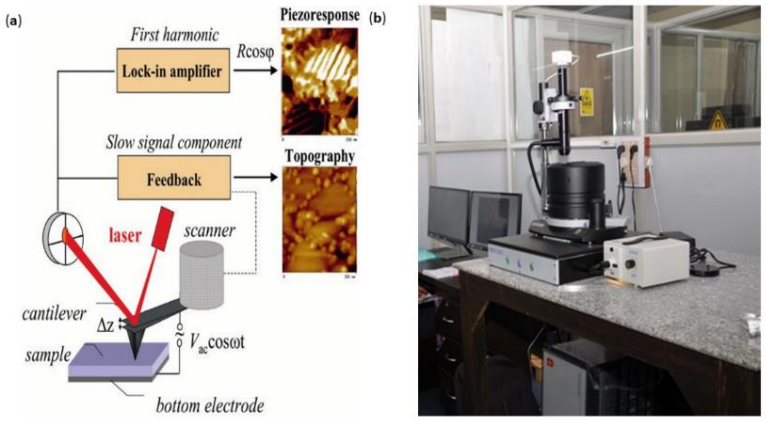

Figure 2.18 (a) Block diagram [188] (b) experimental set up of AFM/PFM at CIF(IITBHU).

2.4.8 DC Poling

The dipoles are assumed to be orientated arbitrarily in a macroscopic crystalline structure that contains many unit cells. When the material experiences mechanical stress, each dipole undergoes rotation from its initial orientation into a direction that minimises the total electrical and mechanical energy stored in the dipole.

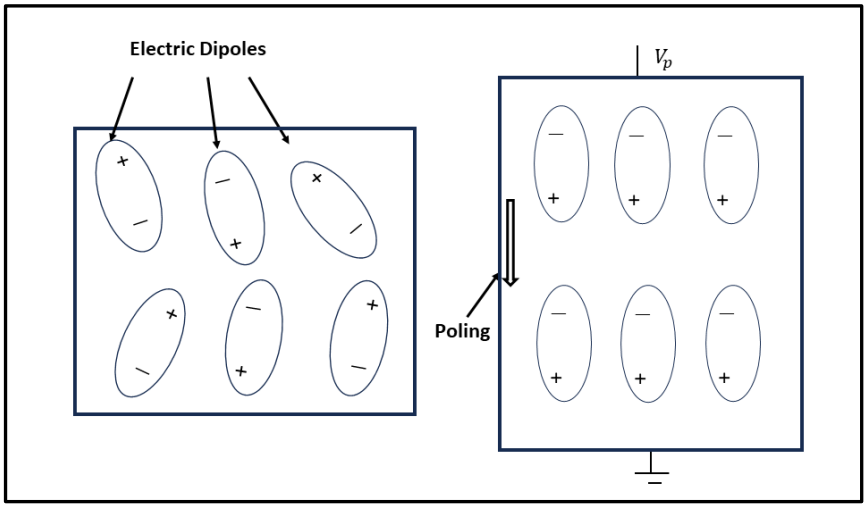

Figure 2.19 Random alignment of dipoles before poling(left) and single order alignment of dipole after poing(right) [189].

If the dipoles are originally randomly orientated, there is no net polarisation, the rotation of the dipoles may not have a substantial impact on the overall polarisation of the material.

Therefore, it is essential to establish an initial state in the material in such a way that the majority of the dipoles will be orientated in a direction that is somewhat consistent with one another. The material can be given such an initial state via the process of poling. The orientation in which the dipoles align is referred to as the poling direction

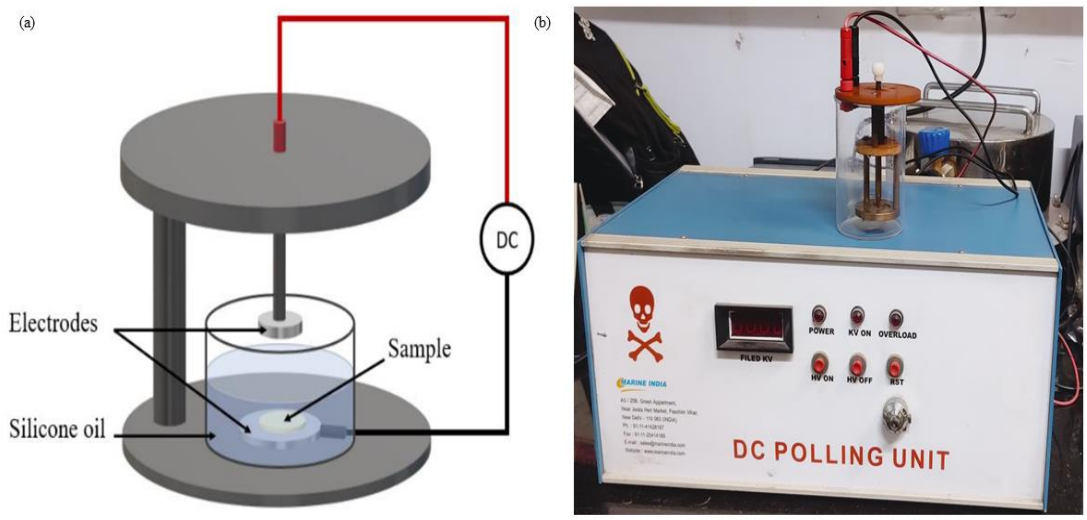

Figure 2.20 (a) Schematic of dc poling unit [190] (b) experimental setup of dc poling unit.

During poling, the material is subjected to a very strong electric field (Figure 2.19), which causes all of the dipoles to point in the same direction. Most dipoles do not revert to their original orientation after switching off the electric field due to the pinning effect caused by tiny imperfections in the crystalline lattice. This produces a material with multiple tiny dipoles that are roughly orientated in the same direction. It is important to note that the material can lose its polarisation if it is exposed to a strong electric field in the opposite direction of its original polarisation or if it is heated above the Curie temperature. The poling procedure was conducted in a silicon oil bath to prevent the occurrence of electrical breakdown in the air.

To study the effect of DC polarisation on the photo-field induced current voltage (I-V) hysteresis area of the green polymorph of $CsSnI_3$, we poled the samples using DC poling unit[190] (Figure 2.20(b)) at 300 K at 0.5 kV/mm duration of 1 h.

2.4.9 Pyroelectric Effect

Pyroelectricity is described as the ability of chosen materials to produce a transient voltage or current when heated or cooled[191]. Sir David Brewster named the term "Pyroelectric effect" in 1824. As a consequence of the change in temperature, the positions of the atoms inside the crystal structure undergo a slight alterations, which ultimately leads to a modification in the polarisation of the material that is being considered. The modification in polarisation results in the generation of a voltage across the crystal. Byer and Roundy [192] suggest that the pyroelectric coefficient (p) can be calculated using the collected current in materials

$$p = \frac{I}{A\frac{dT}{dt}} \tag{2.12}$$

where I is the current running through the pyroelectric materilas, A is the area of the electrode, and $\frac{dT}{dt}$ is the rate of temperature change of temperature. Fig gives the working mechanism of pyroelectric effect (a) Pyroelectric materials have dipole moments that, when added together, produce a spontaneous polarisation; (b) Pyroelectric material that is placed between the two conductive electrodes of a capacitor. In the steady state, the temperature is constant and there is no electric current. (c) an increase in temperature leads to a decrease in spontaneous polarisation, and decrease in temperature results in an increase in spontaneous polarisation.

In the current work, to understand the effect of local polarization on the current-voltage hysteresis study, we perform temperature-dependent pyroelectric current measurements using a Pyro measurement system (Keithley 6517B electrometer) and a temperature-controlled furnace (Figure 2.22)

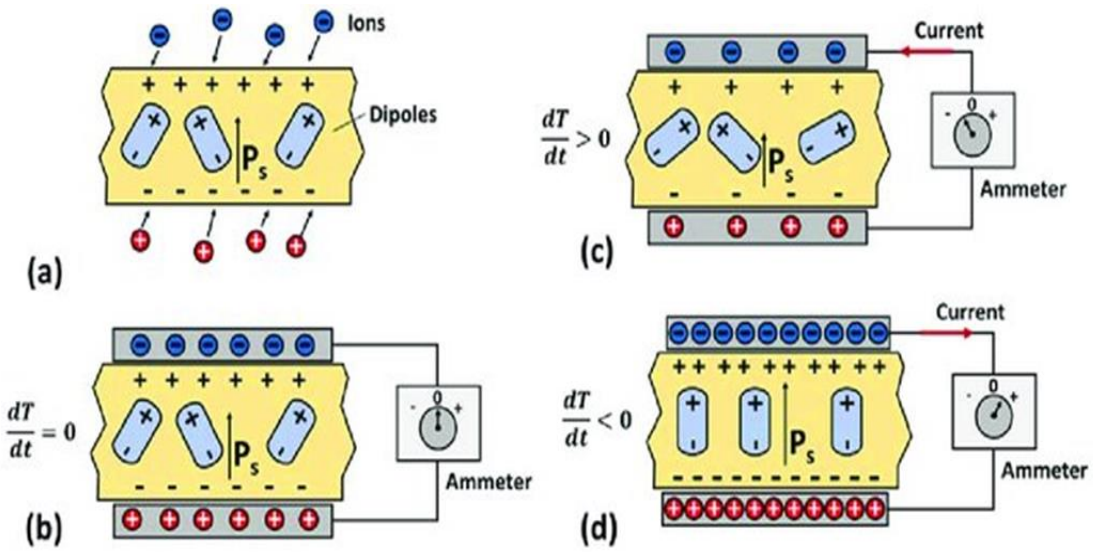

Figure 2.21 An illustration of a pyroelectric generator concept[193].

Figure 2.22 Pyroelectric measurement system (Keithely 6517B electrometer).

2.5 Electrical Properties

2.5.1 Current-Voltage (*I-V*)

The Keithley 2450 source metre is utilised to measure the current-voltage (I-V) curve of synthesised samples. This measurement is performed using an AM 1.5 G filter and the samples are irradiated with a high collimated beam from the Science Tech Solar Simulator of Class AAA, as indicated in Figure 2.23.

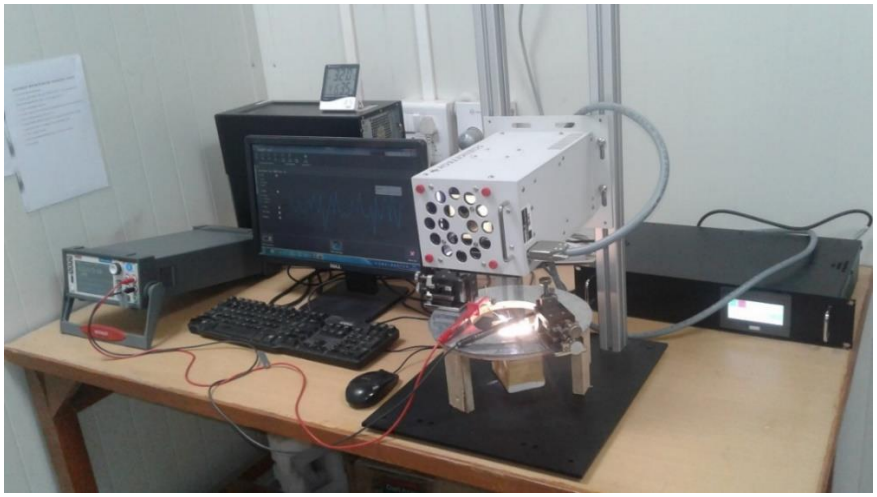

Figure 2.23 An experimental setup of a solar simulator with a Keithley source meter.

The current volatege curve of all the sample are measured under light (AM1.5 G) and dark condition in transverse mode at a fixed scan rate of 1.66 V s^{-1} in dual sweep mode . In addition, to explore the influence of phase transition in the sample ($CsSnI_3$) on current-voltage hysteresis, we studied the temperature-dependent behavior of the current-voltage curve both in the dark and under light (i.e., AM 1.5 G) around the phase transition.

(a) Source Meter: The Keithley 2450 is an advanced source metre or source measurement unit (SMU) equipment that accurately measures Ohm's law (voltage,

current, and resistance) with precise accuracy. A source metre functions as both a direct current (DC) power supply and a digital multi-meter. It is a versatile instrument that is frequently used for nanoscale devices and materials, electrical characterisation of semiconductors, organic semiconductors, low-power devices, and other small geometries. This source metre serves as an ohmmeter, voltage metre, current metre, current source, and voltage source. The device is equipped with a five-inch touch screen that has a high resolution and is sensitive to touch. It has a measuring accuracy of 0.012% and a resolution of 6.5 digits. The front panel is equipped with input banana jacks, while the rear panel features input triaxial connections. The voltage range of the Keithley 2450 is from 20 millivolts to 200 volts, while the current range is from 10 nanoamperes to 1 ampere. There are multiple techniques to measure sweep, including linear, log, dual linear, dual log, and custom.

(b) Solar Simulator: It emits a natural radiance that is comparable to sunlight. The primary goal of this technology is to provide a regulated indoor testing environment commonly found in laboratories. This method enables the separation of photovoltaic parameters. The solar simulator can also be used to expose various materials, gadgets, and plastics to sunlight for testing purposes.

There are three primary components of a solar simulator:

1. Light sources, such as lamps, and power sources
2. Optics and optical filters are used to modify the beam to achieve specific characteristics
3. Operational control components

Several different kinds of lamps, including metal halide, xenon, quartz tungsten halogen, and light-emitting diode-based lamps, were utilised as light sources in solar simulators. However, the xenon arc lamp provides a strong and unfiltered spectrum that closely resembles sunlight. There are two parts to radiation: direct radiation, which originates from the sun, and dispersed radiation, which comes from other parts of the sky and is reflected back to Earth. The Solar Simulator gives the spectral composition of sunlight for various settings and the spectral composition derived from a modified and enhanced xenon lamp source utilising air mass (AM) filters. It is possible to imitate the direct radiation spectrum by utilising a direct filter, which is denoted by the letter 'D'.

2.6 Impedance Spectroscopic Technique

The impedance spectroscopy technique is used to determine the electrical properties of the synthesised material. The conductivity, dielectric permittivity, impedance, and modulus properties of the material can be determined by delivering an alternating voltage or current to the material. The dielectric and electrical properties of polycrystalline materials are influenced by three main factors: (i) the bulk or grains of the material, (ii) the grain boundaries and (iii) the interface between the specimen and the electrode, also known as electrode polarization [194]. To understand electrical behaviour and modify its properties, it is necessary to separate these contributions. These distinct contributions can be identified using impedance analysis, which is present in the electrical or dielectric properties of any electronic. Impedance analysis is a key tool for studying the microstructure, defects, electrical conductivity, and surface chemistry of materials, including ionic conductors and dielectrics. The AC response of any material can be described using four immittance functions. These are complex impedance (Z^*),

electric modulus (M^*), admittance (Y^*) and permittivity ε^*). These are related to each other as[195]:

$$M^* = M' + iM'' = \frac{1}{\varepsilon^*} \tag{2.13}$$

$$\varepsilon^* = \varepsilon' - i\varepsilon'' \tag{2.14}$$

$$Z^* = Z' - iZ'' = \frac{1}{i\omega C_0 \varepsilon^*} \tag{2.15}$$

$$Y^* = Y' + iY'' = i\omega C_0 \varepsilon^* \tag{2.16}$$

The correlation between all of these functions is shown below.

$$D = \tan\delta = \frac{\varepsilon''}{\varepsilon'} = \frac{M''}{M'} = \frac{Y'}{Y''} = \frac{Z'}{Z''} = \frac{\sigma'}{\sigma''} \tag{2.17}$$

$$Z' = \frac{D^2}{G(1+D^2)}, \tag{2.18}$$

$$Z'' = \frac{Z'}{D} \tag{2.19}$$

$$\sigma' = \omega\varepsilon_0\varepsilon'' \text{ and } \sigma'' = \omega\varepsilon_0\varepsilon' \tag{2.20}$$

The variables f, ω (where ω is equal to $2\pi f$) and C_0 represent the frequency (in cycles per second), angular frequency and geometrical capacitance respectively. The frequency-dependent real and imaginary components of the modulus, permittivity, impedance, and admittance are denoted by M', ε', Z', Y', and $M^{"}$, $\varepsilon^{"}$, $Z^{"}$, $Y^{"}$, respectively. Also, Z^*, M^*, and Y^* functions are commonly used for electronic materials.

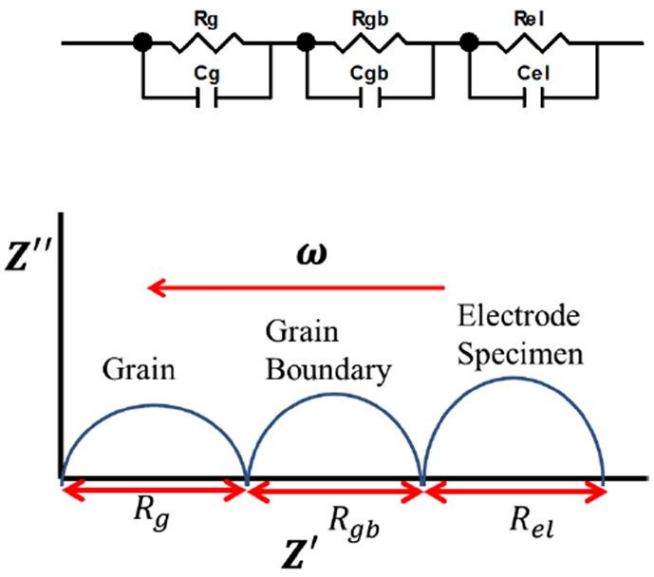

Figure 2.24 The frequency response of the equivalent circuit and its complex impedance plot.

Impedance analysis often uses two types of plots. (1) Complex plane plots, such as $Z^{"}$versus Z' and $M^{"}$ vs M' and (2) Spectroscopic plots, such as, $\frac{Z^{"}}{Z'}$ or $\frac{M^{"}}{M'}$ vs logυ graphs. If a polycrystalline sample contains all three components grains, grain boundaries and electrodes each component can be represented by an analogous circuit consisting of a parallel connection of resistance (R) and capacitance (C).

Therfore, sample can be represented by an equivalent circuit consisting of three parallel RC circuits coupled in series, as illustrated in figure 2.18. The Nyquist plot (Cole-Cole) plot, is mainly utilised to determine the frequency response characteristics of a system by using the complex impedance function: $Z^*(\omega) = Z'(\omega) - iZ''(\omega)$, where the real and imaginary parts of $Z^*(\omega)$ are denoted by $Z'(\omega)$ and $Z^{"}(\omega)$, respectively. The real (Z') and imaginary ($Z^{"}$) components of the total impedance of the analogous circuit are as follows.

$$Z' = \frac{R_g}{(1+\omega R_g C_g)^2} + \frac{R_{gb}}{(1+\omega R_{gb} C_{gb})^2} \qquad (2.21)$$

$$Z'' = R_g \frac{\omega R_g C_{gb}}{(1+\omega R_g C_g)^2} + R_{gb} \frac{\omega R_{gb} C_{gb}}{(1+\omega R_{gb} C_{gb})^2} \quad (2.22)$$

Where R_g is the grain (bulk) resistance, C_g is the grain capacitance, and C_{gb} and R_{gb} are the corresponding grain boundary values. Low-frequency regions are contributed to by grain, whereas high-frequency regions are contributed to by grain border. The interfacial boundary, also known as the grain boundary, has a greater relaxation time compared to the bulk. The relaxation time (τ) can be calculated as the reciprocal of the angular frequency (ω) at which the relaxation peaks occur. This can be expressed as the product of the resistance (R) and the capacitance (C), commonly known as the RC product

$$\tau = 1/\omega = RC \quad (2.23)$$

In this thesis, the powder samples were pelletized using hydraulic press of a diameter of either 12 mm and 6 mm and a thickness of 1 mm. These pellets were then used for electrical measurements.

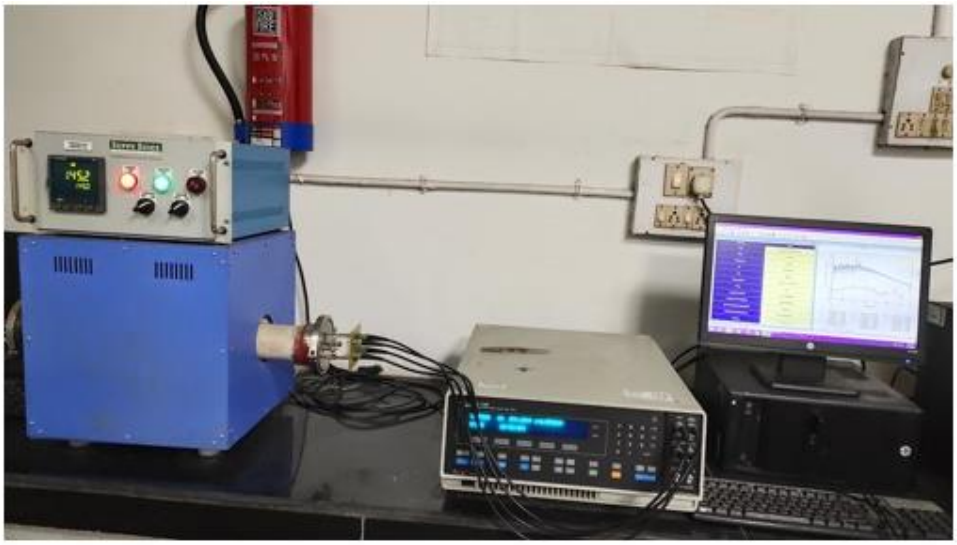

Figure 2.25 Represents the experimental Solartron 1260 A impedance analyzer with sample holder and furnace.

The electrode was made of silver paste, and the silver-coated pellets were measured in the air using two probe techniques at a frequency ranging from 20 Hz to1 MHz.In addition, the impedance of the perovskite material was measured using a Solartron 1260 A impedance analyzer (Figure 2.25).

2.7 Analysis Techniques

2.7.1 Rietveld Refinement Technique

The structural information of the studied materials in the current work is a crucial tool for a more detailed understanding of their properties. X-ray diffraction is the most effective and frequently implemented method among a variety of analysis tools. R. M. Rietveld presents a technique for the refinement of structure parameters that can be applied to powder diffraction data of neutron radiation and X-rays. Rietveld refinement is a powerful method for investigating structural data of sample. Rietveld's refinement method effectively separates these overlapping data and enables an accurate evaluation of the structure. Several aspects of material structure can be defined using the parameters of these reflections, such as height, width, and position. Least-square refinement was used in this process to get the best fit between the theoretical profile and the measured profile. Thus, applying the Rietveld refinement method to a powder X-ray diffraction pattern can yield a lot of information about the material's structure factors. Powder diffraction reflection shape is affected by experimental setup, beam properties, sample size, and shape. A Gaussian shape has been produced as a result of the convolution of the various effects that have been initiated for the monochromatic neutron sources[196]. If this distribution has been taken into consideration, then the contribution of a specific reflection to the profile y_i at position $2\theta_i$ is as follows:

$$y_i = I_k \exp\left[\frac{-4\ln(2)}{H_k^2}(2\theta_i - 2\theta_k)^2\right] \quad (2.24)$$

Where Hk represents the full width at half peak height, also known as the full-width half-maximum (FWHM), $2\theta_k$ represents the centre of the reflex, and I_k represents the calculated intensity of the reflex, which is obtained from the Lorentz factor, the structure factor, and the multiplicity of the reflection. Reflection can become asymmetric due to the vertical divergence of the beam at very low diffraction angles. In order to account for this asymmetry, Rietveld incorporated a semi-empirical correction factor.

$$A_s = 1 - \left[\frac{sP\,(2\theta_i - 2\theta_k)^2}{tan\theta_k}\right] \quad (2.25)$$

The width of the diffraction peaks is increases at higher Bragg angle.This angular dependency was previously described by

$$H_k^2 = U\tan^2\theta_k + V\tan\theta_k + W \quad (2.26)$$

where Rietveld refinement can be used to refine the half-width parameters (U, V, and W) during the fitting process. Rietveld refinement is used to find the function M that represents the difference between the measured data y(obs) and a profile that was calculated y(calc). The expression is defined as:

$$M = \sum_i W_i \left\{y_i^{obs} - \frac{1}{c} y_i^{calc}\right\}^2 \quad (2.27)$$

where c and Wi represent the overall scale factor and statistical weight, such that

$$y^{calc} = cy^{obs} \quad (2.28)$$

The following are the primary characteristics and benefits of the FullProf software:

1. This software can be employed to refine the X-ray diffraction data collected by laboratory set-up and synchrotron sources, as well as neutron diffraction sources.

2. The backgrounds are determined by a range of functions, such as constant functions and higher-order polynomials achieved using Fourier filtering.

3. The peak shape is represented by many functions for each phase, including Lorentzian, Gaussian, pseudo-Voigt, modified Lorentzian, Pearson-VII, split pseudo-Voigt, Thompson-Cox Hashing (TCH) pseudo-Voigt, numerical, and the convolution of a double exponential with a TCH pseudo-Voigt.

4.The Rietveld refinement is capable of analysing numerous phases, with a maximum limit of 16 phases.

5.There are two sorts of functions that can be used to model the preferred orientation of a peak.

6. There are absorption corrections available for a variety of geometries, as well as a micro-absorption correction for the Bragg Brentano set-up.

7. It offers the option of automatically generating hkl and/or symmetry operators.

Refinement of the magnetic structure is another option that can be executed.

9. Automatically generates reflections for incommensurate structures with up to 24 propagation vectors.

10. The position changes of Bragg reflections depend on certain types of defects.

11. Quantitative analysis was done without structural factor calculations.

12. The microstructural analysis can be performed when the instrumental resolution function (Voigt function) is saved in a file.

13. Anisotropic crystallite size and strain can be incorporated into the Popa-Balzer model.

14. To enhance the comparison between the generated pattern and the experimental pattern, the square root of intensity is graphed versus 2θ.

The Rietveld refinement method employs an iterative approach to minimise various structural and microstructural parameters during the fitting of X-ray diffraction profiles. The approaches minimise the difference between experimental intensities (I_{oi}) and estimated intensities (U_{ci}) by refining and adjusting various parameters. The following residual parameters are used to determine the quality of fit. The residual of structure factor-

$$R_F = \frac{\sum_i |\sqrt{I}_{oi} - \sqrt{I}_{ci}|}{\sum_i |\sqrt{I_{oi}}|} \tag{2.29}$$

The residue of Bragg facto

$$R_B = \frac{\sum_i |I_{oi} - I_{ci}|}{\sum_i |I_{oi}|} \tag{2.30}$$

The residue of weighted pattern

$$R_{wp} = \left| \frac{\sum_i W_i (I_{oi} - I_{ci})^2}{\sum_i W_i (I_{oi})^2} \right|^{1/2} \tag{2.31}$$

The residue of expected pattern

$$R_{exp} = \left| \frac{N - P}{\sum_i W_i (I_{oi})^2} \right| \tag{2.32}$$

in all equations The intensity of i^{th} Bragg reflection at the end of the refinement is denoted by I_i. The letter *I* in the suffix represent the observed and estimated intensities.W_i and *N* indicate the weight and quantity of experimental observations, while *P* indicates the number of refinable parameters. The refinement procedure has been continued until convergence of this parameter is achieved. The "Goodness of Fit" (GoF) is also used to monitor the quality of the fit, which is defined as :

$$GoF = \frac{R_{wp}}{R_{exp}} \tag{2.33}$$

The GoF for best fit is approximately 1.00, indicating that the computed and experimental patterns were fully matched.

In this thesis, the Rietveld refinement is performed using the 'Fullprof Suite' software.

2.7.2 Process of Analyzing the Obtained Data

OriginPro 8.5 software was used to analyse the sample's electrical, structural, and optical properties. Additionally, Image-J software was utilised to analyse the grain size distribution using SEM micrographs. Diamond 3.2 software was utilised for the crystal structure of the synthesised sample.

2.8 Conduction Mechanisms

In the present thesis, Bound capacitance model and Frenkel–Poole conduction mechanism has been used to understand the current-voltage (*I-V*) hysteresis behaviors.

2.8.1 Poole-Frenkel

It has been employed to better understanding of the trapping and de-trapping processes of the synthesised material. This mechanism is extremely similar to that of Schottky emission. Poole–Frenkel is also known as internal Schottky emission because it allows thermally excited electrons to escape from the trap and flow into the dielectric[197]. The Poole-Frenkel relation is expressed as[198].

$$\sigma_E = k_2\, e^{-\beta \varepsilon_{trap}} \tag{2.34}$$

$$k_2 = q\mu N_c\, e^{\left(-\frac{\beta \Delta E_{cB,vB}}{2}\right)} \tag{2.35}$$

$$\varepsilon_{trap} = q(\phi_B - \sqrt{(qk_e/\varepsilon_r)E} \tag{2.36}$$

The change of the relative dielectric constant was determined by calculating the slope ($E^{1/2}$ versus $ln\sigma$) of the F-P fitting during both forward and reverse scanning using current-voltage data.